Available online at www.sciencedirect.com

ScienceDirect

Nuclear Physics B 952 (2020) 114915

NUCLEAR PHYSICS B

www.elsevier.com/locate/nuclphysb

Study of a tri-direct littlest seesaw model at MOMENT

Jian Tang, Tse-Chun Wang *

School of Physics, Sun Yat-Sen University, Guangzhou 510275, China

Received 23 September 2019; received in revised form 16 December 2019; accepted 30 December 2019
Available online 9 January 2020
Editor: Tommy Ohlsson

Abstract

The flavour symmetry succeeds in explaining the current global fit results. Flavour-symmetry models can be tested by the future experiments that improve the precision of neutrino oscillation parameters, *such as* the MuOn-decay MEdium baseline NeuTrino beam experiment (MOMENT). In this work, we consider tri-direct littlest seesaw (TDLS) models for a case study, and analyze how much MOMENT can extend our knowledge on the TDLS model. We find that measurements of θ_{23} and δ are crucial for MOMENT to exclude the model at more than 5σ confidence level, if the best fit values in the last global analysis result is confirmed. Moreover, the 3σ precision of model parameters can be improved at MOMENT by at least a factor of two. Finally, we project the surface at the 3σ confidence level from the model-parameter space to the oscillation-parameter space, and find the potential of MOMENT to observe the sum rule between θ_{23} and δ predicted by TDLS.

1. Introduction

The discovery of neutrino oscillations points out the fact that neutrinos have mass, and provides evidence beyond the Standard Model (BSM). This phenomenon is successfully described by a theoretical framework with the help of three neutrino mixing angles (θ_{12}, θ_{13}, θ_{23}), two mass-square splittings (Δm^2_{21}, Δm^2_{31}), and one Dirac CP phase (δ) [1–4]. Thanks to the great efforts in the past two decades, we almost have a complete understanding of such a neutrino

* Corresponding author.
E-mail addresses: tangjian5@mail.sysu.edu.cn (J. Tang), wangzejun@mail.sysu.edu.cn (T.-C. Wang).

https://doi.org/10.1016/j.nuclphysb.2020.114915

oscillation framework. More data in the neutrino oscillation experiments is needed to determine the sign of Δm^2_{31}, to measure the value of $\sin\theta_{23}$, to discover the potential CP violation in the leptonic sector and even to constrain the size of δ [4]. For these purposes, the on-going long baseline experiments (LBLs), such as the NuMI Off-axis ν_e Appearance experiment (NOνA) [5] and the Tokai-to-Kamioka experiment (T2K) [6], can answer these questions with the statistical significance $\gtrsim 3\sigma$ in most of the parameter space. Based on the analysis with their data, the normal mass ordering ($\Delta m^2_{31} > 0$), the higher θ_{23} octant ($\theta_{23} > 45°$), and $\delta \sim 270°$ are preferred so far [4]. The future LBLs, Deep Underground Neutrino Experiment (DUNE) [7], Tokai to Hyper-Kamiokande (T2HK) [8], and the medium baseline reactor experiment, the Jiangmen Underground Neutrino Observatory (JUNO) [9,10] will further complete our knowledge of neutrino oscillations.

The MuOn-decay MEdium baseline NeuTrino beam experiment (MOMENT) has been proposed and is under consideration. Apart from superbeam neutrino experiments like DUNE or T2HK, it is planned to be at muon-decay accelerator neutrino experiments. In such experiments, neutrinos come from a three-body decay process, avoiding intrinsic electron-flavor neutrino contaminations in the reconstructed signals from the source. In addition, MOMENT [11] is likely to use a Gd-doped water Cherenkov detector, which is capable of detecting multiple channels. MOMENT is understood to have excellent properties to study BSM physics, *e.g.* the invisible ν_3 decay [12], NSIs [13–15] and sterile neutrinos [16–19]. Though the current studies on MOMENT have mainly focused on other BSM physics [20,21], it is also necessary to perform physics study related to the standard neutrino oscillation to test the flavour symmetry models.

Flavour symmetry models are used to explain the origin of the neutrino mixing, and to predict the value of oscillation parameters (some of useful review articles are [22–28]). These models are motivated by some interesting features, *such as* $\theta_{12} \sim 33°$, and $\theta_{23} \sim 45°$. Before the discovery of non-zero θ_{13} measurement by Daya Bay experiment [29], the 'tri-bi-maximal' neutrino mixing (TBM) ansatz, which was proposed in 2002 by Horrison, Perkins, and Scott [30], fitted with the experimental data in a good agreement:

$$U_{\rm TBM} = \begin{pmatrix} 2/\sqrt{6} & 1/\sqrt{3} & 0 \\ -1/\sqrt{6} & 1/\sqrt{3} & 1/\sqrt{2} \\ 1/\sqrt{6} & -1/\sqrt{3} & 1/\sqrt{2} \end{pmatrix}.$$

With the fact that $\theta_{13} \approx 8°$, several ways to obtain such non-zero value of θ_{13} are proposed. One of popular proposals is to correct the tri-bi-maximal neutrino mixing such that

$$\sin\theta_{12} = (1+s)/\sqrt{3},\ \ \sin\theta_{13} = r/\sqrt{2},\ \text{ and }\ \sin\theta_{23} = (1+a)/\sqrt{2}.$$

Th neutrino mixing ansatz can be realised by high-energy symmetries G_f. The symmetry of discrete groups G_f, preserved at the high energy but slightly broken at the lower energy, predicts the neutrino mixing, mass-square splittings, and the CP violation phase (Dirac and Majorana phases), with reduced degrees of freedom. The symmetries need to be broken at the low energy. Otherwise, the flavour of leptons cannot be distinguished. There are several approaches for the symmetry breaking, including the direct, indirect, and semi approaches. The direct approach preserves the residual symmetries of G_f in the charged-lepton or neutrino sector. On the other hand, there is no residual symmetry preserved in neither charged-lepton nor neutrino sector in the indirect approach. In the semi approach, the charged-lepton and neutrino sectors preserve different residual symmetries, respectively. This symmetry is broken by extending the Higgs sector or introducing the flavons. To achieve the δ prediction, many models are based on a discrete family symmetry G_f together with a non-commuting CP symmetry $H_{\rm CP}$. Broken in

different approaches, the symmetry $G_f \otimes H_{\rm CP}$ can predict different patterns for the neutrino mixing. For example, in the semi-direct approach, S_4 is preserved in the leading order, and leads the bimaximal (MB) or tri-bimaximal (TB) neutrino mixing, while the higher order terms bring the correction to the neutrino mixing.

One of the most predictive flavour-symmetry models is the littlest seesaw model (LSS), which includes two massive right-handed neutrinos: one corresponds to the atmospheric-mass term, while the other is included for the solar-mass term [31–33]. The littlest seesaw model in the tri-direct approach (TDLS) has been proposed and succeeds in describing the current global-fit results [34,35]. The tri-direct approach is that after the breaking of the family symmetry $G_f \otimes H_{\rm CP}$, three residual symmetries are preserved in different sectors: one in the charged-lepton sector, two in the sectors of right-handed neutrinos for atmospheric and solar mass terms, respectively. In this model, four parameters x, η, r, m_a are used to describe neutrino oscillations. This model has been studied with simulated data at NOνA, T2K, DUNE, T2HK and JUNO [36]. In this work, we study how the next-generation neutrino project using muon-decay beams such as MOMENT can further extend our knowledge on the TDLS model. We have two reasons to motivate this study. Firstly, TDLS describes the current data successfully and tends to be a nice way to offer neutrino mass terms from theoretical point of view. Secondly, it must be straightforward to test the underlying model predictions and compare the performance of MOMENT to the other experiments, *such as* NOνA, T2K, DUNE, and T2HK.

This paper is arranged as follows. In Sec. 2, we will introduce how TDLS models predict oscillation parameters, before presenting how this model describes the NuFit4.0 result. In Sec. 3, we will introduce the statistics and simulation details used in this paper. We will show the definition of χ^2, including the way that we implement "the pull method" to estimate the impact of systematic uncertainties, and how we include the current global-fit results by priors. We will then summarize the assumed configurations for the MOMENT experiment, and will show how the probabilities for MOMENT will be changed by varying each of model parameters. The simulation results will be shown in Sec. 4. We will present the model exclusion capability at MOMENT and how model parameters can be constrained by MOMENT data. We will discuss results of projecting the 3σ sphere from the model-parameter space to the standard-parameter space. Finally, we will close up this paper in Sec. 5 with our conclusions.

2. Model review: littlest Seesaw in the Tri-Direct approach

The littlest seesaw model in the tri-direct approach is currently proposed, and succeeds in describing the current neutrino-oscillation data [34]. In this model, the atmospheric and solar flavon vacuum alignments are $\langle \phi_{\rm atm} \rangle \propto \left(1, \omega^2, \omega\right)^T$ and $\langle \phi_{\rm sol} \rangle \propto (1, x, x)^T$, where $\omega = e^{2\pi i/3}$ stands for a cube root of unity and the parameter x is real because of the imposed CP symmetry. As a result, the Dirac neutrino mass matrix reads as follows:

$$m_D = \begin{pmatrix} y_a & y_s \\ \omega y_a & x y_s \\ \omega^2 y_a & x y_s \end{pmatrix}. \tag{1}$$

The right-handed neutrino Majorana mass matrix is diagonal

$$m_N = \begin{pmatrix} M_{\rm atm} & 0 \\ 0 & M_{\rm sol} \end{pmatrix}. \tag{2}$$

Under the littlest seesaw model, the light left-handed Majorana neutrino mass matrix is given by

Table 1
A summary of the relation between oscillation parameters and TDLS model parameters [34]. Two requirements are imposed by TDLS: the smallest mass state $m_1 = 0$ and the normal mass ordering. The sign of $\sin\delta$ depends on the sign of $x\cos\psi$: "+" ("−") is for $x\cos\psi > 0$ (< 0).

Model parameters	x, η, $r(\equiv m_s/m_a)$, m_a
Combinations of model parameters	$y = \frac{5x^2+2x+2}{2(x^2+x+1)}(m_a + e^{i\eta}m_s)$, $z = -\frac{\sqrt{5x^2+2x+2}}{2(x^2+x+1)}\left[(x+2)m_a - x(2x+1)e^{i\eta}m_s\right]$, $w = \frac{1}{2(x^2+x+1)}\left[(x+2)^2 m_a + x^2(2x+1)^2 e^{i\eta}m_s\right]$, $\sin\psi = \frac{\Im(y^*z+wz^*)}{\lvert y^*z+wz^*\rvert}$, $\cos\psi = \frac{\Re(y^*z+wz^*)}{\lvert y^*z+wz^*\rvert}$. $\sin 2\theta = \frac{2\lvert y^*z+wz^*\rvert}{\sqrt{(\lvert w\rvert^2-\lvert y\rvert^2)^2+4\lvert y^*z+wz^*\rvert^2}}$, $\cos 2\theta = \frac{\lvert w\rvert^2-\lvert y\rvert^2}{\sqrt{(\lvert w\rvert^2-\lvert y\rvert^2)^2+4\lvert y^*z+wz^*\rvert^2}}$.
Oscillation parameters	$\Delta m^2_{21} = m_2^2 = \frac{1}{2}\left[\lvert y\rvert^2 + \lvert w\rvert^2 + 2\lvert z\rvert^2 - \frac{\lvert w\rvert^2-\lvert y\rvert^2}{\cos\theta}\right]$, $\Delta m^2_{31} = m_3^2 = \frac{1}{2}\left[\lvert y\rvert^2 + \lvert w\rvert^2 + 2\lvert z\rvert^2 + \frac{\lvert w\rvert^2-\lvert y\rvert^2}{\cos\theta}\right]$, $\sin^2\theta_{12} = 1 - \frac{3x^2}{3x^2+2(x^2+x+1)\cos^2\theta}$, $\sin^2\theta_{13} = \frac{2\left(x^2+x+1\right)\sin^2\theta}{5x^2+2x+2}$, $\sin^2\theta_{23} = \frac{1}{2} + \frac{x\sqrt{3(5x^2+2x+2)}\sin 2\theta\sin\psi}{2\left[3x^2+2(x^2+x+1)\cos^2\theta\right]}$, $\cos\delta = \frac{\cot 2\theta_{23}\left[3x^2-\left(4x^2+x+1\right)\cos^2\theta_{13}\right]}{\sqrt{3}\lvert x\rvert\sin\theta_{13}\sqrt{(5x^2+2x+2)\cos^2\theta_{13}-3x^2}}$, $\sin\delta = \pm\csc 2\theta_{23}\sqrt{1 + \frac{\left(x^2+x+1\right)^2\cot^2\theta_{13}\cos^2 2\theta_{23}}{3x^2\left[3x^2\tan^2\theta_{13}-2\left(x^2+x+1\right)\right]}}$.

$$m_\nu = m_a\begin{pmatrix} 1 & \omega & \omega^2 \\ \omega & \omega^2 & 1 \\ \omega^2 & 1 & \omega \end{pmatrix} + e^{i\eta}m_s\begin{pmatrix} 1 & x & x \\ x & x^2 & x^2 \\ x & x^2 & x^2 \end{pmatrix}, \tag{3}$$

where $m_a = |y_a^2/M_{\rm atm}|$, $m_s = |y_s^2/M_{\rm sol}|$, and the only physically important phase η depends on the relative phase between $y_a^2/M_{\rm atm}$ and $y_s^2/M_{\rm sol}$. The parameter r is defined the ratio of m_s to m_a, $r \equiv m_s/m_a$. Obviously, from Eq. (3), $m_1 = 0$ and the normal mass ordering are imposed by TDLS. We summarise the dependence of oscillation parameters on model parameters in Table 1. Ref. [34] further predicts the sum rule for TDLS,

$$\cos^2\theta_{12}\cos^2\theta_{13} = \frac{3x^2}{5x^2+2x+2}\,. \tag{4}$$

We use the best fit value and the 3σ uncertainty of NuFit4.0 [4] (shown in Table 2), we find the best fit results for TDLS models in Table 3. The 3σ uncertainty is given as

$$\begin{aligned} &-5.475 < x < -3.37,\ 0.455 < \eta/\pi < 1.545, \\ &0.204 < r < 0.606,\ 3.343 < m_a/\text{meV} < 4.597. \end{aligned} \tag{5}$$

Table 2
The best fit and 3σ uncertainty, in the results of NuFit4.0 [4].

Parameter	$\theta_{12}/^\circ$	$\theta_{13}/^\circ$	$\theta_{23}/^\circ$	$\delta/^\circ$	$\Delta m^2_{21}/10^{-5}\text{eV}^2$	$\Delta m^2_{31}/10^{-3}\text{eV}^2$
best fit	33.82	8.61	49.6	215	7.39	2.525
3σ Range	$31.61 - 36.27$	$8.22 - 8.99$	$40.3 - 52.4$	$125 - 392$	$6.79 - 8.01$	$2.47 - 2.625$

Table 3
The best fit for x, η, r, m_a with the result of NuFit4.0 [4], and the corresponding oscillation parameters.

$\Delta\chi^2$	x	η/π	r	m_a/ meV	$\theta_{12}/^\circ$	$\theta_{13}/^\circ$	$\theta_{23}/^\circ$	$\delta/^\circ$	$\Delta m^2_{21}/10^{-5}\text{eV}^2$	$\Delta m^2_{31}/10^{-3}\text{eV}^2$
4.98	−3.65	1.13	0.511	3.71	35.25	8.63	46.98	278.96	7.39	2.525

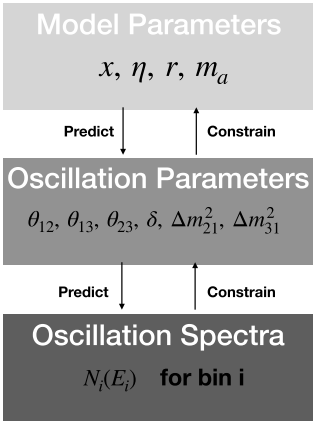

Fig. 1. A scheme to correlate the model parameters with standard neutrino oscillation parameters. The error propagation is implemented in the simulation code up to the spectra analysis.

Notable between Tables 2 and 3 is that the most inconsistent oscillation parameters are θ_{23} and δ. The others are placed within the 1σ error, or even at the best-fit value (*e.g.* Δm^2_{21} and Δm^2_{31}). As a result, we are looking forward to improving precision measurements on θ_{23} and δ for further understanding of this model.

3. Simulation details

3.1. Statistics method

The statistical study on the TDLS model at MOMENT can be understood in Fig. 1. The model imposes correlations between or among the standard neutrino oscillation parameters, and predicts the oscillation spectra for MOMENT. In other words, the neutrino spectra of MOMENT can constrain the standard oscillation parameters, and therefore test the TDLS model or constrain the model parameters. Based on this perspective, we use two methods to conduct the numerical analysis with the simulated data:

- The standard three neutrino oscillations expressed by three mixing angles, two mass-square splittings and one Dirac-CP phase: $\overrightarrow{\mathcal{O}} = \{\theta_{12}\,, \theta_{13}\,, \theta_{23}\,, \delta_{\text{CP}}\,, \Delta m^2_{21}\,, \Delta m^2_{31}\}$. We expect that

precision measurements of mixing parameters are correlated with uncertainties of current global fit results. We suppose that a given experiment reconstructs neutrino spectra in N bins sequentially. The number of observed events in the bin i is recorded as n_i, which in our work is predicted by the true model. We can build a $\chi^2_{st.}(\vec{\mathcal{O}})$ to quantify the sensitivity:

$$\chi^2_{st.}(\vec{\mathcal{O}}) = \sum_{i=1}^{N} \left[\frac{\mu_i(\vec{\mathcal{O}}) - n_i}{\sigma_i} \right]^2 , \tag{6}$$

where μ_i is the number rate of bin i predicted by the hypothesis $\vec{\mathcal{O}}$.

- We consider the following parameters from TDLS: $\vec{\mathcal{M}} = \{x\,, \eta\,, m_a\,, r\}$. Other steps in the likelihood analysis will follow the same strategy as the above method, but replace the Eq. (6) with

$$\chi^2_{st.}(\vec{\mathcal{M}}) = \sum_{i=1}^{N} \left[\frac{\mu_i(\vec{\mathcal{O}}(\vec{\mathcal{M}})) - n_i}{\sigma_i} \right]^2 , \tag{7}$$

with standard oscillation parameters as a function of model parameters $\vec{\mathcal{O}}(\vec{\mathcal{M}})$.

To describe the impact of systematic uncertainties, we adopt the following modification:

$$\chi^2_{sys.}(\vec{\mathcal{O}} \text{ or } \vec{\mathcal{M}}) = \min_{\{\xi_s, \xi_b\}} \sum_{i=1}^{N} \left[\frac{\mu_i((\vec{\mathcal{O}} \text{ or } \vec{\mathcal{O}}(\vec{\mathcal{M}});\ \xi_s, \xi_b) - n_i}{\sigma_i} \right]^2 + p(\xi_s, \sigma_s) + p(\xi_b, \sigma_b)\,, \tag{8}$$

where $p(\xi, \sigma) = \xi^2/\sigma^2$ is a Gaussian prior on the nuisance parameter ξ with the uncertainty σ (subscripts s and b denote signal and background respectively) and $\mu_i((\vec{\mathcal{O}} \text{ or } \vec{\mathcal{O}}(\vec{\mathcal{M}});\ \xi_s, \xi_b)$ is predicted event rate for bin i

$$\mu_i((\vec{\mathcal{O}} \text{ or } \vec{\mathcal{O}}(\vec{\mathcal{M}});\ \xi_s, \xi_b) = (1 + \xi_s) \times \mu_{s,i} + (1 + \xi_b) \times \mu_{b,i}, \tag{9}$$

with the signal rate $\mu_{s,i}$ and the background rate $\mu_{b,i}$ for each energy bin i.

To include the currently constraints for the neutrino oscillation parameters, we finally use

$$\chi^2(\vec{\mathcal{O}} \text{ or } \vec{\mathcal{M}}) = \min_{\vec{\mathcal{O}} \text{ or } \vec{\mathcal{M}}} \chi^2_{sys.}(\vec{\mathcal{O}} \text{ or } \vec{\mathcal{M}}) + \sum_i p(\vec{\mathcal{O}}_i(\vec{\mathcal{M}}), \vec{\mathcal{O}}_{cen.,i}, \vec{\sigma}_i)\,, \tag{10}$$

where $\sum_i p(\vec{\mathcal{O}}_{hyp.}, \vec{\mathcal{O}}_{cen.}, \vec{\sigma})$ is the summation of Gaussian priors over all oscillation parameters with two vectors: one includes all central values $\vec{\mathcal{O}}_{cen.}$ and the other consists of the standard deviation $\vec{\sigma}$. The values for $\vec{\mathcal{O}}_{cen.}$ and $\vec{\sigma}$ are taken from the best-fit value and according to 3σ uncertainties of the NuFit4.0 result [4] (shown in Table 2), respectively. In this work, the values of $\vec{\mathcal{O}}(\vec{\mathcal{M}})$ are predicted by the TDLS model.

3.2. Experiment setting

We summarize the simulation details for MOMENT in Table 4. MOMENT, as a medium muon decay accelerator neutrino experiment, has been originally proposed as a future experiment

Table 4
Assumptions for the source, detector and the running time at MOMENT in the simulation. The energy resolution is described by a Gaussian distribution with the width σ_E.

MOMENT	
Fiducial mass	Gd-doping Water cherenkov (500 kton)
Channels	$\nu_e(\bar{\nu}_e) \to \nu_e(\bar{\nu}_e)$, $\nu_\mu(\bar{\nu}_\mu) \to \nu_\mu(\bar{\nu}_\mu)$, $\nu_e(\bar{\nu}_e) \to \nu_\mu(\bar{\nu}_\mu)$, $\nu_\mu(\bar{\nu}_\mu) \to \nu_e(\bar{\nu}_e)$
Energy resolution σ_E	$8.5\% \times E$
Runtime	μ^- mode 5 yrs + μ^+ mode 5 yrs
Baseline	150 km
Energy range	100 MeV to 800 MeV
Normalization	appearance channels: 2.5%
(error on signal)	disappearance channels: 5%
Sources of	Neutral current, Atmospheric neutrinos
Background	Charge misidentification

to measure the leptonic CP-violating phase, though it also has good sensitivities on θ_{13}, θ_{23} and Δm^2_{31} [37].

The neutrino fluxes are kindly provided by the MOMENT working group [11]. The events are taken from 100 to 800 MeV. We assume five-year data taken at the μ^- and μ^+ mode, respectively. Eight oscillation channels ($\nu_e \to \nu_e$, $\nu_e \to \nu_\mu$, $\nu_\mu \to \nu_e$, $\nu_\mu \to \nu_\mu$ and their CP-conjugate partners) are considered in this work. Multi-channel analyses are helpful in measuring the values of multiple parameters. As a result, the detector design is also crucial to precisely read out the events from different neutrino-oscillation channels. We have to consider flavour and charge identifications to distinguish secondary particles by means of an advanced neutrino detector — a 500 kton Gd-doped water cherenkov detector. The charged-current interactions are used to identify neutrino signals: $\nu_e + n \to p + e^-$, $\bar{\nu}_\mu + p \to n + \mu^+$, $\bar{\nu}_e + p \to n + e^+$, and $\nu_\mu + n \to p + \mu^-$, with the new technology using Gd-doped water to separate both Cherenkov and coincident signals from capture of thermal neutrons [38,39]. The energy resolution is assumed $12\%/E$ for all channels. For the systematic uncertainties, we assume $\sigma_s = 2.5\%$ for signal normalizations and $\sigma_b = 5\%$ for background fluctuations.

The major background components come from the atmospheric neutrinos, neutral current backgrounds and charge mis-identifications. They can be largely suppressed with the beam direction and a proper modelling background spectra during the beam-off period, which are to be extensively studied in detector simulations. We consider matter effects during neutrino propagations with the help of the Preliminary Reference Earth Model (PREM) density profile is considered in the numerical calculations [40].

3.3. Neutrino oscillation probabilities in the TDLS model

In Figs. 2 and 3, we present the variation of probabilities for MOMENT with the 3σ uncertainty for model parameters in terms of NuFit4.0 results given in Eq. (5). We also show the probability with the best fit values as the input Table 3. In Fig. 2, we see the variation of ν_μ and $\bar{\nu}_\mu$ disappearance channels is much larger than those in the electron neutrino disappearance channels. As a result, ν_μ and $\bar{\nu}_\mu$ disappearance channels are two most dominating channels for the TDLS model. In the lower two panels, we see the variation of x in the model has the largest impact, covering the range from 0 to 1 for the probability within 0.1 GeV $\leq E_\nu \leq$ 0.8 GeV.

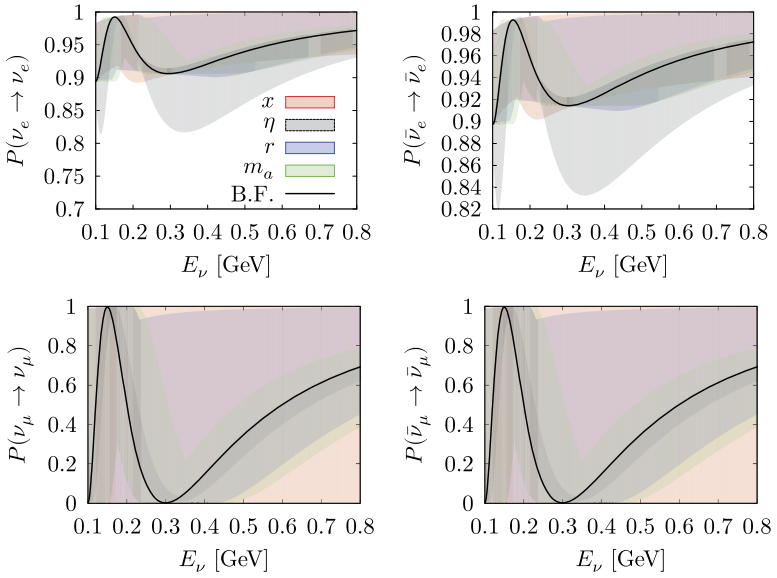

Fig. 2. The impact of the probability for varying each model parameters within 3σ uncertainty predicted with Nu-Fit4.0 result Eq. (5): $-5.475 < x < -3.37$ (red band), $0.455 < \eta/\pi < 1.545$ (dark grey band), $0.204 < r < 0.606$ (blue band), $3.343 < m_a/\text{meV} < 4.597$ (green band). We also show the probability for the best fit (B.F.) Table 3 in the black curve: $(x,\ \eta,\ r,\ M_a) = (-3.65,\ 1.13\pi,\ 0.511,\ 3.71\ \text{meV})$. The upper left (right) panel is for $P(\nu_e \to \nu_e)$ ($P(\bar{\nu}_e \to \bar{\nu}_e)$), while the lower left (right) panel is for $P(\nu_\mu \to \nu_\mu)$ ($P(\bar{\nu}_\mu \to \bar{\nu}_\mu)$). (For interpretation of the colours in the figure(s), the reader is referred to the web version of this article.)

The second largest effect comes from the model parameter r. It also ranges from 0 to 1, yet the trend is different. For the higher energy ($E_\nu > 0.45$ GeV), the lower bound of the probability is getting larger, and it is ~ 0.45 at $E_\nu = 0.8$ GeV for both channels. For the model parameter m_a, the probability is changing with $\Delta P \sim 0.2$ along with the probability for the best fit value in Table 3. The similar feature is seen for the parameter η; yet the variation of probability is smaller $\Delta P \sim 0.05$. It seems that η is the distinctive parameter not to be measured by ν_μ and $\bar{\nu}_\mu$ disappearance channels as easily as the other three model parameters. Eventually, we find that ν_e and $\bar{\nu}_e$ disappearance channels are more sensitive to the variation of η than the other parameters, where ΔP can approach ~ 0.1 around the first minimum $E_\nu \sim 0.3$ GeV.

In Fig. 3, we show variations of $P(\nu_\mu \to \nu_e)$, $P(\bar{\nu}_\mu \to \bar{\nu}_e)$, $P(\nu_e \to \nu_\mu)$, and $P(\bar{\nu}_e \to \bar{\nu}_\mu)$. The behaviours in four panels are almost the same. The largest variation is given by the impact of η: $\Delta P \sim 0.06$ around the first maximum $E_\nu \sim 0.3$ GeV for all panels. The impact of model parameters x and r can reduce the lower bound significantly in the probability plane. From the first minimum to 8 GeV, the lower bound of probability can even reach 0. For both parameters, the variation of probability is around $\Delta P \sim 0.03$. The variation for m_a is the smallest around 0.01.

We observed that the lower limits reach 0 in a wide range of E_ν for most of channels, except ν_e and $\bar{\nu}_e$ disappearance ones. This happens when we varying the values of x and r. The reason for this feature is that the oscillation minimum moves in wide range of E_ν with x or r, as we see in Fig. 4, in which we use $P(\nu_\mu \to \nu_e)$ as an example. We vary x from -5.5 to -3.5 (left panel), and vary r from 0.2 to 0.6 (right panel). The result demonstrates that the horizontal shift of the minimum makes the lower limit of the band to be 0 in a wide E_ν region.

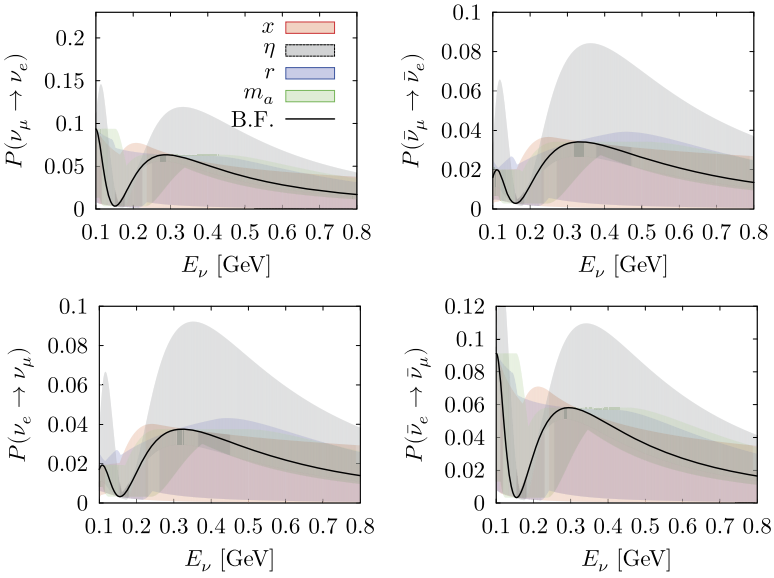

Fig. 3. The impact of the probability for varying each model parameters within 3σ uncertainty predicted with Nu-Fit4.0 result Eq. (5): $-5.475 < x < -3.37$ (red band), $0.455 < \eta/\pi < 1.545$ (dark grey band), $0.204 < r < 0.606$ (blue band), $3.343 < m_a/\text{meV} < 4.597$ (green band). We also show the probability for the best fit (B.F.) Table 3 in the black curve: $(x,\ \eta,\ r,\ m_a) = (-3.65,\ 1.13\pi,\ 0.511,\ 3.71\ \text{meV})$. The upper left (right) panel is for $P(\nu_\mu \to \nu_e)$ ($P(\bar{\nu}_\mu \to \bar{\nu}_e)$), while the lower left (right) panel is for $P(\nu_e \to \nu_\mu)$ ($P(\bar{\nu}_e \to \bar{\nu}_\mu)$).

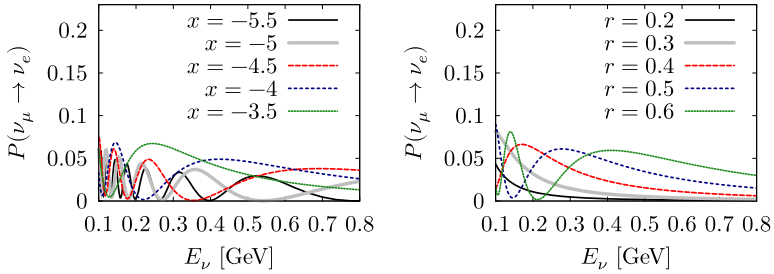

Fig. 4. The impact of the probability $P(\nu_\mu \to \nu_e)$ for varying value for x (left) and r (right). Except for the varied one, the other parameters are used according to Table 3 in the black curve: $(x, \eta, r, m_a) = (-3.65, 1.13\pi, 0.511, 3.71\ \text{meV})$. In the left (right) panel, the black, thick grey, red-dashed, blue-short-dashed, and green-dotted curves are $x = -5.5, -5, -4.5, -4, -3.5$ ($r = 0.2, 0.3, 0.4, 0.5, 0.6$), respectively.

To sum up, we see that ν_μ and $\bar{\nu}_\mu$ disappearance channels are the most important channels to constrain TDLS models, especially for x, r and m_a. However, the other six channels can provide information for η. Thanks to the multiple channel features, MOMENT can be used to study TDLS models and can even measure model parameters precisely.

4. Results

In this section, we present physics potentials of MOMENT on the TDLS model. We firstly predict the exclusion limit for this model in different scenarios. We will see that θ_{23} and δ are

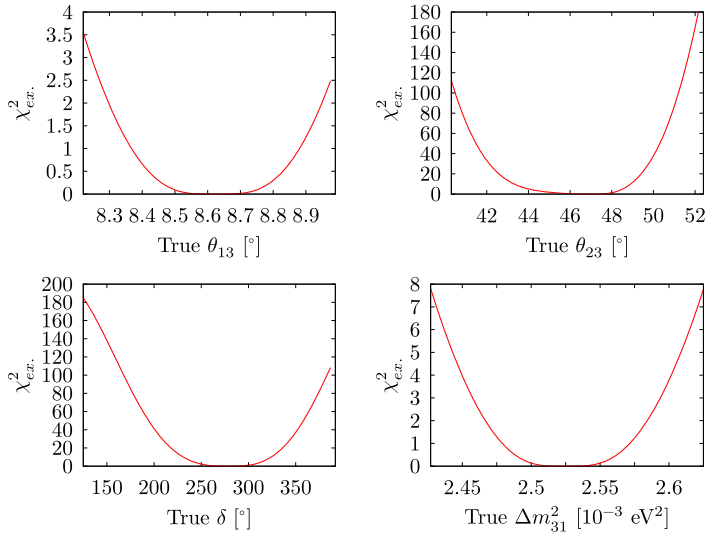

Fig. 5. The $\chi^2_{ex.}$ value for tri-direct littlest seesaw model for θ_{13}, θ_{23}, δ and Δm^2_{31}. The range for each parameter is taken according to the 3σ uncertainty in NuFit4.0 results.

key parameters to exclude TDLS models. Then, we study how MOMENT data can be used to constrain model parameters. We will see model-parameter degeneracies due to the poor measurement of θ_{12}. We also project the $\Delta\chi^2$ to θ_{23}-δ plane from the model parameter space. This shows an interesting correlation and demonstrates the goodness of fit in the analysis of simulated data.

4.1. Model exclusion

To give the model exclusion curves, we study the minimum of χ^2 value for the TDLS with a given set of true values for the standard oscillation parameters (three mixing angles, two mass-square splittings, and a Dirac CP phase), and define the statistical quantity $\chi^2_{ex.}$ as follows:

$$\chi^2_{ex.} = \sum_i \min_{\vec{\mathcal{M}}} \chi^2(\mu_i(\vec{\mathcal{M}}), n_i(\vec{\mathcal{O}}_{true})). \tag{11}$$

We adopt Wilk's theorem [41]. When comparing nested models, the $\Delta\chi^2$ test statistics is a random variable asymptotically distributed according to the χ^2-distribution with the number of degrees of freedom, which is equal to the difference in the number of free model parameters. The statistical quantity $\chi^2_{ex.}$ can be understood as the minimum of $\Delta\chi^2$ value for given true values for oscillation parameters. And this quantity is exactly $\Delta\chi^2$ value in Table 3.

We present our result in Figs. 5 and 6. In these figures, we vary true values for each one or two of standard oscillation parameters, while the other standard oscillation parameters are fixed at the TDLS predictions (θ_{12}, θ_{13}, θ_{23}, δ, Δm^2_{21}, Δm^2_{31}) $\sim$ (35.25°, 8.63°, 47°, 279°, 7.39×10^{-5} eV^2, 2.525×10^{-3} eV^2). As we do not see any impact on θ_{12} and Δm^2_{21}, we will simply ignore them in our discussion from now on.

In Fig. 5, we show the $\chi^2_{ex.}$ values against various true values for θ_{13} (upper-left), θ_{23} (upper-right), δ (lower-left), Δm^2_{31} (lower-right). The range we show is given by the 3σ uncertainty in the NuFit4.0. Strikingly, we see very high exclusion levels for θ_{23} and δ; for θ_{23} (δ), $\chi^2_{ex.}$ can

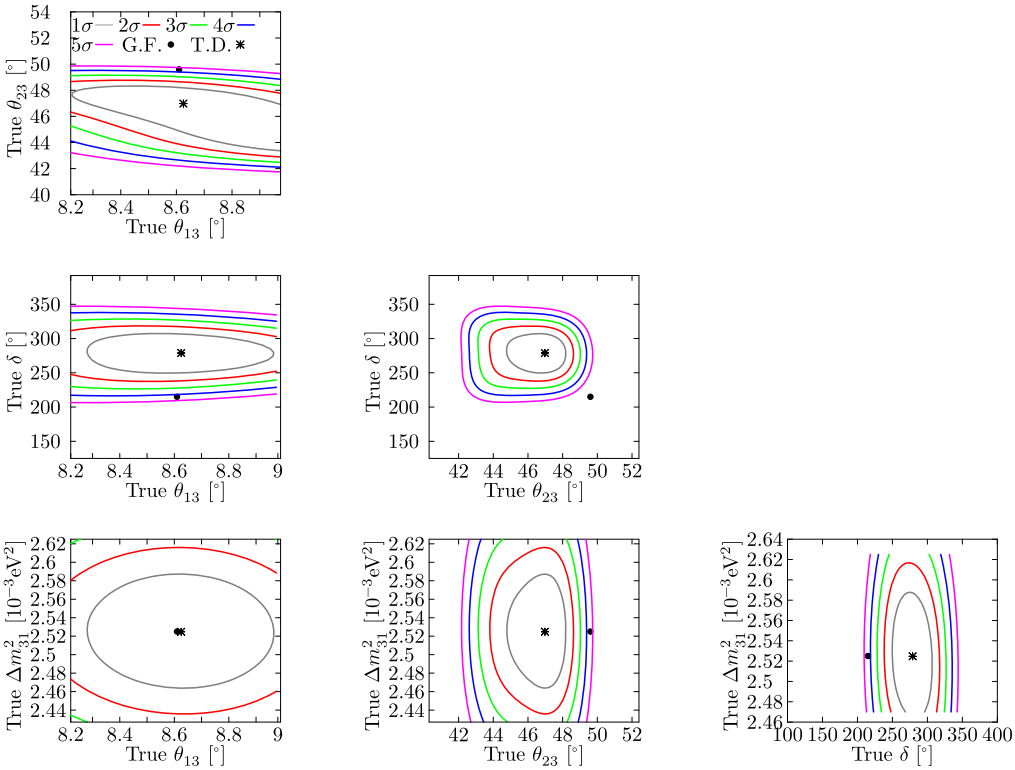

Fig. 6. The 2-D exclusion contour for tri-direct littlest seesaw model on the plane of any two true standard parameters, from 1σ to 5σ. The statistical quantity computed in this figure is $\chi^2_{ex.}$ Eq. (11). The range for each parameter is taken according to the 3σ uncertainty in NuFit4.0 results. The black dot denotes the best fit of NuFit4.0 results $((\theta_{12},\ \theta_{13},\ \theta_{23},\ \delta,\ \Delta m^2_{21},\ \Delta m^2_{31}) = (33.82^\circ,\ 8.61^\circ,\ 49.6^\circ,\ 215^\circ,\ 7.39\times10^{-5}\ \mathrm{eV}^2,\ 2.525\times10^{-3}\ \mathrm{eV}^2))$, while the star is the prediction by the tri-direct littlest seesaw model with NuFit4.0 results $((\theta_{12},\ \theta_{13},\ \theta_{23},\ \delta,\ \Delta m^2_{21},\ \Delta m^2_{31}) \sim (35.25^\circ,\ 8.63^\circ,\ 47^\circ,\ 279^\circ,\ 7.39\times10^{-5}\ \mathrm{eV}^2,\ 2.525\times10^{-3}\ \mathrm{eV}^2))$.

climb up to ~ 160 (~ 120) at the upper bound, and reach ~ 90 (~ 180) at the lower bound. For Δm^2_{31}, the exclusion level $\chi^2_{ex.}$ at both bounds is close to 8. The worst one among these four parameters is θ_{13}, and it cannot even reach 2σ exclusion level at the 3σ uncertainty of NuFit4.0.

In Fig. 6, we show 2-dimension contours at 1σ (gray), 2σ (red), 3σ (green), 4σ (blue), and 5σ (magenta) on a combination of two parameters from θ_{13}, θ_{23}, δ, and Δm^2_{31}. The statistical quantity computed in this figure is $\chi^2_{ex.}$ in Eq. (11), which can be considered as a minimum of $\Delta\chi^2$ for a given true values of oscillation parameters. We vary the true values for two oscillation parameters in order to see if the exclusion ability can be enhanced via the precision measurement of two oscillation parameters. The range we show is the 3σ uncertainty in NuFit4.0. In all panels, the black dot denotes the best fit of NuFit4.0 results $((\theta_{12},\ \theta_{13},\ \theta_{23},\ \delta,\ \Delta m^2_{21},\ \Delta m^2_{31}) = (33.82^\circ,\ 8.61^\circ,\ 49.6^\circ,\ 215^\circ,\ 7.39\times10^{-5}\ \mathrm{eV}^2,\ 2.525\times10^{-3}\ \mathrm{eV}^2))$, while the star is the prediction by the tri-direct littlest seesaw model with NuFit4.0 results $((\theta_{12},\ \theta_{13},\ \theta_{23},\ \delta,\ \Delta m^2_{21},\ \Delta m^2_{31}) \sim (35.25^\circ,\ 8.63^\circ,\ 47.^\circ,\ 279^\circ,\ 7.39\times10^{-5}\ \mathrm{eV}^2,\ 2.525\times10^{-3}\ \mathrm{eV}^2))$. Though we do not see any correlations, we find that the black

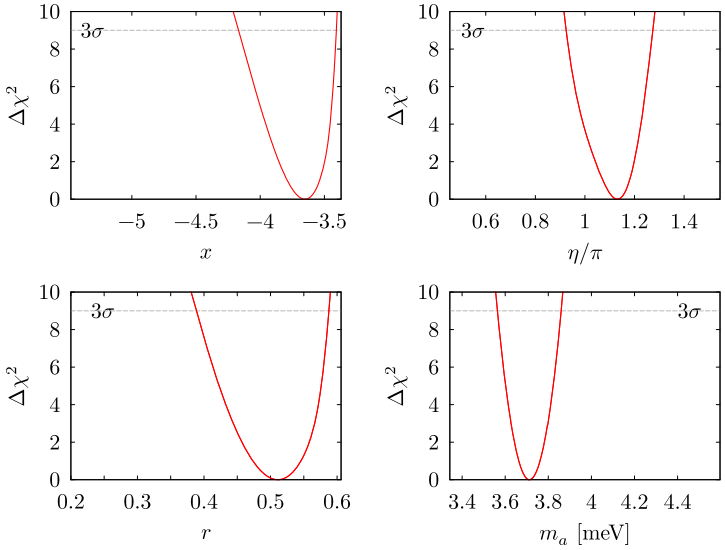

Fig. 7. The $\Delta\chi^2$ value against each model parameters for MOMENT. True values for the model parameters are used $(x,\ \eta,\ r,\ m_a) = (-3.65,\ 1.13\pi,\ 0.511,\ 3.71\ \text{meV})$. The range shown here is according to the 3σ uncertainty with NuFit4.0 results Eq. (5): $-5.475 < x < -3.37$ (red band), $0.455 < \eta/\pi < 1.545$ (dark grey band), $0.204 < r < 0.606$ (blue band), $3.343 < m_a/\text{meV} < 4.597$ (yellow band).

dot is outside of 5σ contour on the θ_{23}-δ plane. This tells us that the measurement of θ_{23} and δ for MOMENT can exclude the TDLS over 5σ if NuFit4.0 results are confirmed.

4.2. Model parameter constraint

We study how model parameters can be constrained by MOMENT. For this purpose, we study the statistics quantity,

$$\Delta\chi^2 = \sum_i \chi^2(\mu_i(\vec{\mathcal{M}}_{hyp.}), n_i(\vec{\mathcal{M}}_{true})) - \sum_i \chi^2(\mu_i(\vec{\mathcal{M}}_{b.f.}), n_i(\vec{\mathcal{M}}_{true})), \tag{12}$$

where $\vec{\mathcal{M}}_{hyp.}$ is the hypothesis, $\vec{\mathcal{M}}_{true}$ is the true values, and $\vec{\mathcal{M}}_{b.f.}$ is the best fit. Here $\vec{\mathcal{M}}_{b.f.}$ is exactly $\vec{\mathcal{M}}_{true}$. We show our result in Figs. 7 and 8. We set the true values at the $(x,\ \eta,\ r,\ m_a) = (-7/2,\ \pi,\ 0.553,\ 3.72\ \text{meV})$, which is the best fit with NuFit4.0 results. And the range for each panel is the 3σ uncertainty with NuFit4.0 results Eq. (5): $-5.475 < x < -3.37$ (red band), $0.455 < \eta/\pi < 1.545$ (dark grey band), $0.204 < r < 0.606$ (blue band), $3.343 < m_a/\text{meV} < 4.597$ (yellow band). At 3σ confidence level, the uncertainty of the model parameter x lies roughly from -4.25 to -3.5. For the model parameter η, it ranges from $\sim 0.925\pi$ to $\sim 1.275\pi$. The 3σ errors for r and m_a are about $0.36 < r < 0.58$ and $3.5\text{meV} < m_a < 3.85\text{meV}$. Compared to the result shown in Eq. (5), we see the parameter with the least improvement is r, for which the 3σ uncertainty is improved by a factor of 2.

In Table 5, we compare our simulated results with those in the current global fit and the other neutrino experiments: the combination of NOνA and T2K, DUNE, and T2HK. For the last three configurations, we take results from Ref. [36]. This is obvious that MOMENT can largely im-

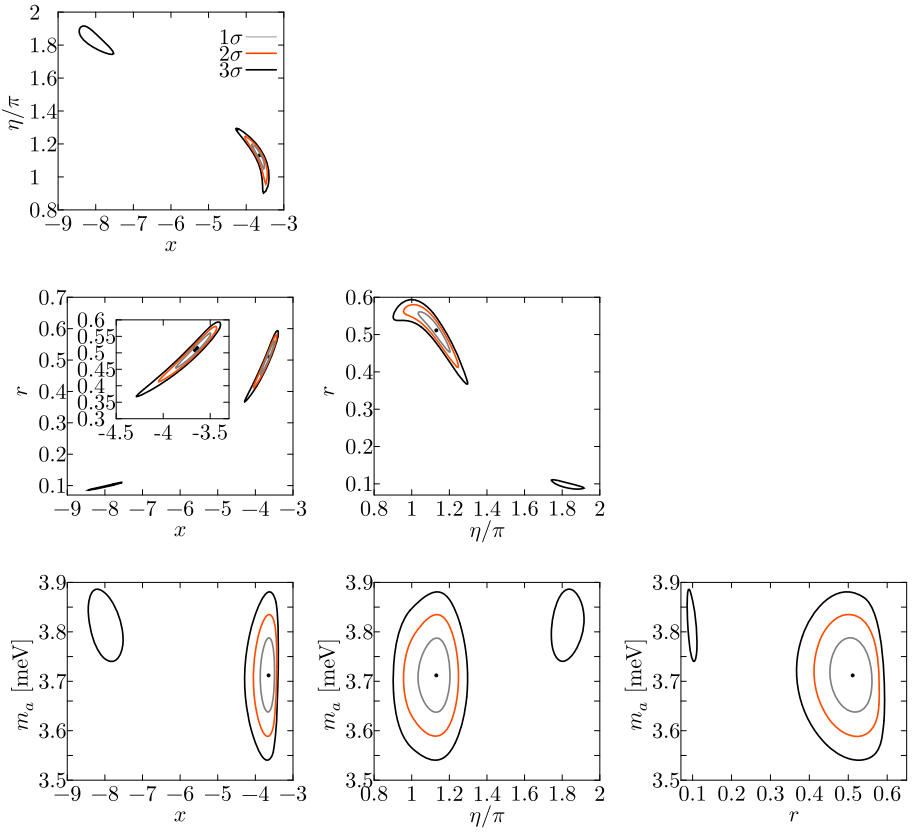

Fig. 8. Precision measurements of any two model parameters in the framework of three neutrino oscillations taking uncertainties of the current global fit results, for MOMENT, at 1σ (gray), 2σ (orange), 3σ (black) confidence level. True values for the model parameters are used $(x,\ \eta,\ r,\ m_a) = (-3.65,\ 1.13\pi,\ 0.511,\ 3.71\ \text{meV})$.

Table 5
The 3σ allowed ranges in x, η, r, m_a for NuFit4.0 [4], MOMENT, the combination of NOνA and T2K, DUNE and T2HK. For the last three configurations, we take the result from Ref. [36].

exp.	x	η/π	r	m_a/meV
NuFit4.0	$[-5.475,\ -3.37]$	$[0.455,\ 1.545]$	$[0.204,\ 0.606]$	$[3.343,\ 4.597]$
MOMENT	$[-4.25,\ -3.5]$	$[0.925,\ 1.275]$	$[0.36,\ 0.58]$	$[3.56,\ 3.86]$
NOνA+T2K	$[-4.8,\ -3.5]$	$[0.84,\ 1.4]$	$[0.3,\ 0.6]$	$[3.56,\ 3.86]$
DUNE	$[-4.2,\ -3.5]$	$[0.93,\ 1.27]$	$[0.4,\ 0.6]$	$[3.56,\ 3.86]$
T2HK	$[-3.8,\ -3.5]$	$[0.94,\ 1.21]$	$[0.45,\ 0.6]$	$[3.56,\ 3.86]$

prove the sensitivity of these model parameters, in contrast to results with simulated NOνA and T2K data ($-4.8 < x < -3.5$, $0.84 < \eta/\pi < 1.4$, $0.3 < r < 0.6$ and $3.56 < m_a/\text{meV} < 3.83$ for 3σ uncertainties). We also find the performance of MOMENT is similar to that of DUNE ($-4.2 < x < -3.5$, $0.93 < \eta/\pi < 1.27$, $0.4 < r < 0.6$ and $3.56 < m_a/\text{meV} < 3.83$ for 3σ un-

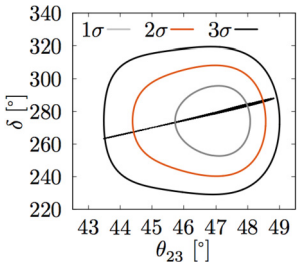

Fig. 9. The points at the 4-dimension sphere at the 3σ projected on θ_{23}-δ for MOMENT experiment. We also present the 1σ (grey), 2σ (orange), and 3σ (black) contours without the restriction of TDLS.

certainties), but worse than that of T2HK ($-3.8 < x < -3.5, 0.94 < \eta/\pi < 1.21, 0.45 < r < 0.6$ and $3.56 < m_a/\text{meV} < 3.86$ for 3σ uncertainties). We cannot neglect the fact that because they are not sensitive to the size of Δm^2_{21}, the 3σ allowed range on m_a is the same to MOMENT, the combination of NOνA and T2K, DUNE, and T2HK.

In Fig. 8, we show 1σ (gray), 2σ (light-orange) and 3σ (black) contours on the plane spanned by any two of model parameters. We see a strong correlation among x, η and r, which is consistent with Eq. (3). In Eq. (3), we see these three parameters joint in the matrix for the neutrino solar mass. As a result these degeneracies can be resolved by precision measurement of solar mixing angle θ_{12} or solar mass-square splitting Δm^2_{21}. This degeneracy problem has also addressed by simulation results in other LBL experimental configurations, and is known to be resolved by the precision measurement of θ_{12} [36].

In Fig. 9, we project the 3σ sphere from the 4-dimension model-parameter space to the plane spanned by θ_{23} and δ. In more detail, we take a point $(x^i, \eta^i, r^i, m^i_a)$ on the 3σ sphere in the space of all four model parameters, and we place this point at $(\theta^i_{12}, \theta^i_{13}, \theta^i_{23}, \delta^i, \Delta m^{2,i}_{21}, \Delta m^{2,i}_{31})$ in the oscillation-parameter space. Two points $(x^i, \eta^i, r^i, m^i_a)$ and $(\theta^i_{12}, \theta^i_{13}, \theta^i_{23}, \delta^i, \Delta m^{2,i}_{21}, \Delta m^{2,i}_{31})$ can be transferred by relations in Table 1. Obviously, this can demonstrate the restriction on oscillation parameters by TDLS, and is a way to understand if MOMENT can be used to observe the sum rule predicted by TDLS. Also, because the degree of freedom is reduced, the precision of oscillation parameters can be better. For the purpose, we also compare the result with the allowed contour without the restriction of TDLS. The band feature appears, assuming TDLS. This feature can be understood by the expansions of $\cos\delta$ and $\sin\delta$ in Table 1:

$$\cos\delta = \frac{\cot 2\theta_{23}\left[3x^2 - \left(4x^2 + x + 1\right)\cos^2\theta_{13}\right]}{\sqrt{3}\,|x|\sin\theta_{13}\sqrt{\left(5x^2 + 2x + 2\right)\cos^2\theta_{13} - 3x^2}}, \tag{13}$$

and

$$\sin\delta = \pm\csc 2\theta_{23}\sqrt{1 + \frac{\left(x^2 + x + 1\right)^2\cot^2\theta_{13}\cos^2 2\theta_{23}}{3x^2\left[3x^2\tan 2\theta_{13} - 2\left(x^2 + x + 1\right)\right]}}, \tag{14}$$

with "+" for $x\cos\psi > 0$ and "−" for $x\cos\psi < 0$.

Considering $\theta_{23} \sim 45°$, we have

$$\begin{aligned} \cos\delta &\propto \cot 2\theta_{23} = \frac{\cos 2\theta_{23}}{\sin 2\theta_{23}}, \\ \sin\delta &\propto \pm\csc 2\theta_{23} = \pm\frac{1}{\sin 2\theta_{23}}. \end{aligned} \tag{15}$$

Therefore, we have

$$\tan\delta \propto 1/\cos 2\theta_{23}. \tag{16}$$

Eq. (16) predicts that if $\theta_{23} = 45°$, $\delta = 90°$ or 270°, which is also confirmed in the θ_{23}-δ panel of Fig. 9. On the other hand, due to the poor sensitivity to the solar angle of MOMENT, we do not see the result reflecting the sum rule in Eq. (4). More results for projecting $\Delta\chi^2$ on the other standard-parameter space are presented in Appendix A.

5. Conclusion

We have studied how we can extend our knowledge on the flavor symmetry with MOMENT, using eight channels of neutrino oscillations ($\nu_e \to \nu_e$, $\nu_e \to \nu_\mu$, $\nu_\mu \to \nu_e$, $\nu_\mu \to \nu_\mu$ and their CP-conjugate partners) with the help of the following detection processes in a Gd-doped water Cherenkov detector: $\nu_e + n \to p + e^-$, $\bar{\nu}_\mu + p \to n + \mu^+$, $\bar{\nu}_e + p \to n + e^+$, and $\nu_\mu + n \to p + \mu^-$. We have analyzed the physics potential of MOMENT on littlest seesaw models in the tri-direct approach given in Eq. (3) as a case study.

We have studied the exclusion ability to TDLS models for MOMENT. We found that θ_{23} and δ are the most important parameters to exclude this model, though some contributions from θ_{13} and Δm^2_{31} are also seen. We noticed that the precision measurement in MOMENT of θ_{23} and δ can exclude this model with more than 5σ significance, if the best fit of NuFit4.0 is confirmed. We also presented the constraint on model parameters with simulated MOMENT data. We have found MOMENT data can improve the 3σ uncertainty by at least a factor of two, compared to those by NuFit4.0 results shown in Eq. (5). We have found the degeneracy problem, which is caused by the poor measurement of θ_{12}. This degeneracy problem has been addressed in Ref. [36]. We projected the 3σ sphere from the model-parameter space to the oscillation-parameter space. Finally, we have found that the sum rule between θ_{23} and δ: $\tan\delta \propto 1/\cos 2\theta_{23}$ (for $\theta_{23} \sim 45°$) predicted by Eqs. (13) and (14) can be checked by MOMENT.

Finally, we come to the conclusion that θ_{23} and δ are the most important parameters in the standard neutrino mixing framework to understand the underlying TDLS model. It is not only because they are the only two parameters, of which the model prediction deviates from the best fit of NuFit4.0 by more than 1σ, but also because they can exclude this model at the 5σ confidence level as soon as the best fit values are confirmed in the future global analysis. As a result, to optimize the experimental design at MOMENT for the purpose of understanding the TDLS model, we need to aim at precision measurements of θ_{23} and δ.

Acknowledgements

This work is supported in part by the National Natural Science Foundation of China under Grant No. 11505301 and No. 11881240247. We appreciate Gui-Jun Ding's great help in understanding the tri-direct symmetry models. We would like to thank the accelerator working group of MOMENT for useful discussions and for kindly providing flux files for the MOMENT experiment. We finally acknowledge Dr. Sampsa Vihonen's help to improve the readability of this paper.

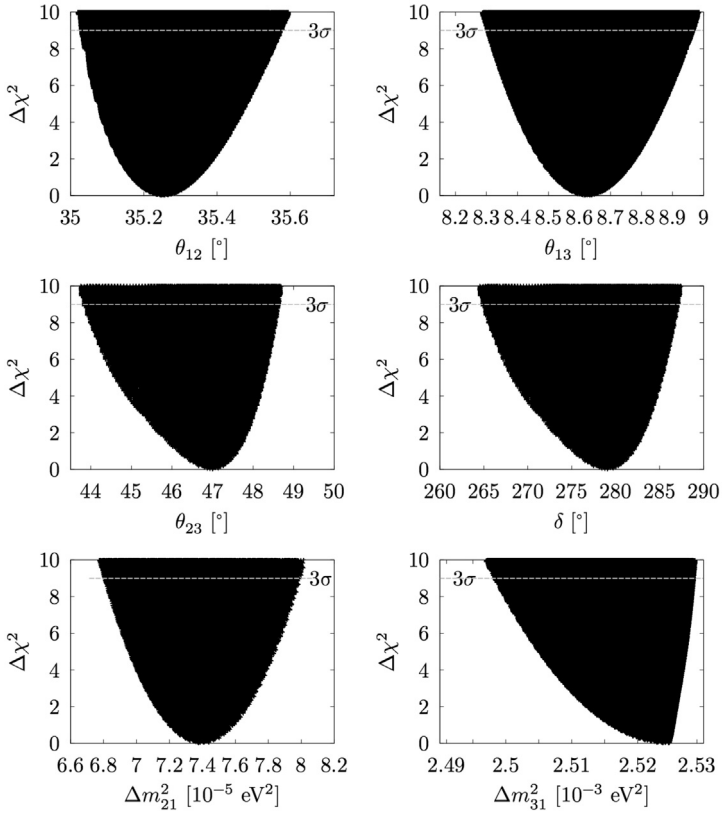

Fig. 10. The $\Delta\chi^2$ value against θ_{12} (upper left), θ_{13} (upper right), θ_{23} (middle left), δ (middle right), Δm^2_{21} (lower left) and Δm^2_{31} (lower right), for MOMENT experiment, assuming the tri-direct model.

Appendix A. Projection on the standard-parameter space

After studying the behaviour of $\Delta\chi^2$ in the model-parameter space (x, η, r and m_a) in Sec. 4.2, we are interested in its behaviour the oscillation-parameter space (θ_{12}, θ_{13}, θ_{23}, δ, Δm^2_{21}, and Δm^2_{31}). Therefore, we project the value of $\Delta\chi^2$ from the model-parameter space to the oscillation-parameter space. In Fig. 10, we will show the $\Delta\chi^2$ against the value of one oscillation parameter, and in Fig. 11, we will project the point on 3σ allowed contour on θ_{13}-δ, θ_{13}-Δm^2_{31}, and θ_{23}-Δm^2_{31} planes.

In Fig. 10, we project points inside the 3σ sphere from the 4-dimension model-parameter space on each oscillation parameters with their $\Delta\chi^2$ values (y-axis). Though MOMENT is not sensitive to θ_{12}, we see that this parameter is well constrained to be better than that of NuFit4.0 result. The uncertainty for θ_{13} and Δm^2_{21} are almost the same as the 3σ errors NuFit4.0. The asymmetry for θ_{12}, θ_{23} and Δm^2_{31} is passed by the same feature of x, η, and m_a.

In Fig. 11, we project the 3σ sphere from the 4-dimension model-parameter space to the two-dimension plane spanned by the standard oscillation parameters. We see that under the TDLS model, δ and Δm^2_{31} are constrained better than those without assuming TDLS models by about a

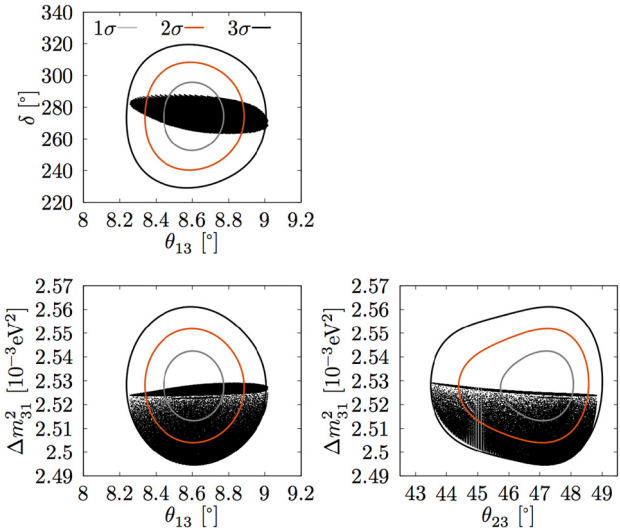

Fig. 11. The points at the 4-dimension sphere at the 3σ projected on θ_{13}-δ (upper-left), θ_{13}-Δm^2_{31} (lower-left), θ_{23}-Δm^2_{31} (lower-right) for MOMENT experiment. We also present the 1σ (grey), 2σ (orange), and 3σ (black) contours without the restriction of TDLS.

factor of 2. The uncertainty for θ_{23} is slightly better when TDLS is assumed. The 3σ uncertainty for θ_{13} is roughly the same between with and without assuming TDLS models.

References

[1] B. Pontecorvo, Sov. Phys. JETP 26 (1968) 984, Zh. Eksp. Teor. Fiz. 53 (1967) 1717.
[2] Z. Maki, M. Nakagawa, S. Sakata, Prog. Theor. Phys. 28 (1962) 870, 34(1962).
[3] B. Pontecorvo, Sov. Phys. JETP 7 (1958) 172, Zh. Eksp. Teor. Fiz. 34 (1957) 247.
[4] I.Esteban, M.C. Gonzalez-Garcia, A. Hernandez-Cabezudo, M. Maltoni, T. Schwetz, J. High Energy Phys. 01 (2019) 106, arXiv:1811.05487.
[5] D.S. Ayres, et al., NOvA, 2007.
[6] K. Abe, et al., T2K, Nucl. Instrum. Methods Phys. Res., Sect. A 659 (2011) 106, arXiv:1106.1238.
[7] R. Acciarri, et al., DUNE, arXiv:1512.06148, 2015.
[8] K. Abe, et al., Hyper-Kamiokande Working Group, arXiv:1412.4673, 2014.
[9] Z. Djurcic, et al., JUNO, arXiv:1508.07166, 2015.
[10] F. An, et al., JUNO, J. Phys. G 43 (2016) 030401, arXiv:1507.05613.
[11] J. Cao, et al., Phys. Rev. Spec. Top., Accel. Beams 17 (2014) 090101, arXiv:1401.8125.
[12] J. Tang, T.-C. Wang, Y. Zhang, J. High Energy Phys. 04 (2019) 004, arXiv:1811.05623.
[13] M.B. Gavela, D. Hernandez, T. Ota, W. Winter, Phys. Rev. D 79 (2009) 013007, arXiv:0809.3451.
[14] F. Bonnet, D. Hernandez, T. Ota, W. Winter, J. High Energy Phys. 10 (2009) 076, arXiv:0907.3143.
[15] M.B. Krauss, T. Ota, W. Porod, W. Winter, Phys. Rev. D 84 (2011) 115023, arXiv:1109.4636.
[16] S. Gariazzo, C. Giunti, M. Laveder, Y.F. Li, J. High Energy Phys. 06 (2017) 135, arXiv:1703.00860.
[17] K.N. Abazajian, et al., arXiv:1204.5379, 2012.
[18] M. Drewes, et al., J. Cosmol. Astropart. Phys. 1701 (2017) 025, arXiv:1602.04816.
[19] P. Minkowski, Phys. Lett. B 67 (1977) 421.
[20] J. Tang, Y. Zhang, Phys. Rev. D 97 (2018) 035018, arXiv:1705.09500.
[21] J. Tang, Y. Zhang, Y.-F. Li, Phys. Lett. B 774 (2017) 217, arXiv:1708.04909.
[22] G. Altarelli, F. Feruglio, Rev. Mod. Phys. 82 (2010) 2701, arXiv:1002.0211.
[23] H. Ishimori, T. Kobayashi, H. Ohki, Y. Shimizu, H. Okada, M. Tanimoto, Prog. Theor. Phys. Suppl. 183 (2010) 1, arXiv:1003.3552.

[24] S.F. King, C. Luhn, Rep. Prog. Phys. 76 (2013) 056201, arXiv:1301.1340.
[25] S.F. King, A. Merle, S. Morisi, Y. Shimizu, M. Tanimoto, New J. Phys. 16 (2014) 045018, arXiv:1402.4271.
[26] S.F. King, J. Phys. G 42 (2015) 123001, arXiv:1510.02091.
[27] S.F. King, Nucl. Part. Phys. Proc. 265–266 (2015) 288.
[28] S.F. King, Prog. Part. Nucl. Phys. 94 (2017) 217, arXiv:1701.04413.
[29] F.P. An, et al., Daya Bay, Phys. Rev. Lett. 112 (2014) 061801, arXiv:1310.6732.
[30] P.F. Harrison, D.H. Perkins, W.G. Scott, Phys. Lett. B 530 (2002) 167, arXiv:hep-ph/0202074.
[31] S.F. King, J. High Energy Phys. 07 (2013) 137, arXiv:1304.6264.
[32] S.F. King, J. High Energy Phys. 02 (2016) 085, arXiv:1512.07531.
[33] S.F. King, C. Luhn, J. High Energy Phys. 09 (2016) 023, arXiv:1607.05276.
[34] G.-J. Ding, S.F. King, C.-C. Li, J. High Energy Phys. 12 (2018) 003, arXiv:1807.07538.
[35] G.-J. Ding, S.F. King, C.-C. Li, Phys. Rev. D 99 (2019) 075035, arXiv:1811.12340.
[36] G.-J. Ding, Y.-F. Li, J. Tang, T.-C. Wang, Phys. Rev. D 100 (2019) 055022, arXiv:1905.12939.
[37] J. Tang, S. Vihonen, T.-C. Wang, arXiv:1909.01548, 2019.
[38] J.-E. Campagne, M. Maltoni, M. Mezzetto, T. Schwetz, J. High Energy Phys. 04 (2007) 003, arXiv:hep-ph/0603172.
[39] T. Ishida, Hyper-Kamiokande Working Group, arXiv:1311.5287, 2013.
[40] A.M. Dziewonski, D.L. Anderson, Phys. Earth Planet. Inter. 25 (1981) 297.
[41] S.S. Wilks, Ann. Math. Stat. 9 (1938) 60.